10.1002/chem.202000125

FULL PAPER

WILEY-VCH

Bottom-up synthesized MoS_2 interfacing polymer carbon nanodots with electrocatalytic activity for hydrogen evolution

Antonia Kagkoura,[a] Ruben Canton-Vitoria,[a] Lorenzo Vallan,[b] Javier Hernandez-Ferrer,[b] Ana M. Benito,[b] Wolfgang K. Maser,[b] Raul Arenal,[c, d, e] and Nikos Tagmatarchis*[a]

Abstract: The preparation of MoS_2-polymer carbon nanodot (MoS_2-PCND) hybrid material was accomplished by employing an easy and fast bottom-up synthetic approach. Specifically, MoS_2-PCND was realized by the thermal decomposition of ammonium tetrathiomolybdate and the in-situ complexation of Mo with carboxylic acid units present in the surface of PCNDs. The newly prepared hybrid material was comprehensively characterized by spectroscopic, thermal and electron microscopy imaging means. The electrocatalytic activity of MoS_2-PCND was examined against the hydrogen evolution reaction (HER) and compared with that attributed to the hybrid material prepared by a top-down approach, namely with MoS_2-PCND(exf-fun), in which MoS_2 was firstly exfoliated and then covalently functionalized with PCNDs. The MoS_2-PCND hybrid material showed superior electrocatalytic activity against HER with low Tafel slope value and excellent electrocatalytic stability, with an onset potential at -0.16 V vs RHE. The superior catalytic performance of MoS_2-PCND was rationalized by considering the catalytic active sites of MoS_2, the effective charge/energy-transfer phenomena from PCNDs to MoS_2 and the synergetic effect between MoS_2 and PCNDs within the hybrid material.

Introduction

Hydrogen is an excellent candidate fuel for renewable energy applications, since it provides a clean and reliable alternative energy source for the disengagement of fossil fuels that are the ruling conventional energy source. Although, hydrogen is the most abundant element on earth, it is hard to be found in a pure form, which means that it needs to be produced by renewable sources. Among numerous practiced techniques for hydrogen production, electrochemical water splitting is a straightforward, inexpensive and highly efficient approach. In order to harvest hydrogen from water electrolysis, electric potential is applied between the anode and cathode, where O_2 and H_2 are produced via two-half reactions of oxygen and hydrogen evolution, respectively.[1, 2] In general, an efficient electrocatalyst should be able to withstand high current density as well as to be resistant to acidic media, in which normally the hydrogen evolution reaction (HER) takes place, and should also exhibit low overpotential, i.e. lowest potential needed for initializing hydrogen evolution and low Tafel slope value. Analysis of the electric current response to the applied potential (Tafel slope) is employed to elucidate the reaction mechanism of the electrocatalysts and provides information associated with the rate determining steps. Experimentally observed Tafel slope values can be compared with the theoretically derived slopes assuming different rate-determining steps based on the kinetic model. Moreover, cost-effectiveness and abundance of the electrocatalyst are of paramount importance for wide usage and commercialization. Up to date, Pt and Pt-based materials are the most efficient electrocatalysts towards HER, since they exhibit almost zero onset potential and zero Gibbs free energy of hydrogen adsorption (ΔG_H).[3] The latter value is extremely important when describing an electrocatalyst. When ΔG_H equals zero maximum HER activity is obtained. More negative ΔG_H values result in stronger binding between hydrogen and the surface of the catalyst and hinder the desorption of H_2 molecules. On the contrary, more positive ΔG_H values are related to weaker binding between hydrogen and the surface of the catalyst, which impedes the proton/electron-transfer step.

The family of carbon nanodots consists of graphitic (GCNDs), carbonaceous (CNDs) and polymeric (PCNDs) types[4] of photoluminescent organic nanoparticles (<10 nm) whose optoelectronic properties are of extreme interest for energy-related applications.[5, 6] Their photochemical stability,[7] solubility in both aqueous and organic solvents[8] and easiness to fabricate with environmental means,[9] has resulted in attracting huge scientific attention during the last two decades. In particular, PCNDs can be easily obtained starting from cheap and chemically simple precursors, such as citric acid and polyamines,[10] which are polymerized together by means of heating,[11,12] acid treatment[13] or employment of catalysts.[14] A photo-induced intramolecular charge transfer process between localized molecular states takes place on the polymeric structure of PCNDs, originating strong fluorescent emission.[15] This behavior has been fruitfully exploited for the implementation of PCNDs in donor-acceptor materials[16] and for the preparation of prototype solar cells[13] and LEDs.[17]

On the other hand, molybdenum disulfide MoS_2 is a well-studied transition metal dichalcogenide (TMD) which has proven to be an auspicious material for HER due to its inherent electrocatalytic properties.[18-21] Depending on the agent employed for the exfoliation and the number of electrons of the

[a] Dr. A. Kagkoura, Dr. R. Canton-Vitoria, Dr. N. Tagmatarchis
Theoretical and Physical Chemistry Institute
National Hellenic Research Foundation
48 Vassileos Constantinou Avenue, Athens 11635, Greece.
E-mail: tagmatar@eie.gr
[b] Dr. L. Vallan, Dr. J. Hernandez-Ferrer, Dr. A. M. Benito, Dr. W. K. Maser
Instituto de Carboquimica, (ICB-CSIC)
C/Miguel Luesma Castan 4, E-50018, Zaragoza, Spain.
[c] Dr. Raul Arenal
Laboratorio de Microscopias Avanzadas (LMA), Instituto de Nanociencia de Aragon (INA), Universidad de Zaragoza, Mariano Esquillor s/n, 50018 Zaragoza, Spain.
[d] Dr. Raul Arenal
Instituto de Ciencias de Materiales de Aragon, CSIC-U. de Zaragoza, Calle Pedro Cerbuna 12, 50009 Zaragoza, Spain.
[e] Dr. Raul Arenal
ARAID Foundation, 50018 Zaragoza, Spain.

Supporting information for this article is given via a link at the end of the document.

transition metal that fill the d-orbitals, TMDs display various symmetries, i.e. trigonal prismatic D_{3h} symmetry possessing semiconducting properties, while octahedral O_h coordination exhibiting metallic properties.[22] Specifically, the natural abundance of MoS_2, together with the low cost, near zero positive Gibbs free energy ($\Delta G_H \sim 0.06eV$)[19,23] and effectiveness for HER in strong acidic environments, which is a prerequisite for efficient electrocatalytic reactions, gives MoS_2 a head start as Pt-free electrocatalyst. Several approaches have been developed for improving the density of accessible edges at the surface of TMDs since catalytic activity is believed to originate from unsaturated chalcogen atoms at the edges. These strategies involve modification of the surface of TMDs in order to maximize edge sites.[24,25] Alternatively, edge sites can be created by introducing structural defects on the surface of the catalysts.[26-28] Another way to improve TMDs' electrocatalytic activity towards HER is by phase engineering. Compared to semiconducting 2H-MoS_2, which has limited active sites located at the edges and exhibits high electrical resistance, metallic 1T-MoS_2 shows a dramatic improvement in HER performance since both basal plane and edges are catalytically active.[29-31] Furthermore, 1T-MoS_2 exhibits much higher conductivity allowing improved electron transfer. At the same time, hybridization with conductive substrates, such as graphene can further increase electron transfer and subsequently promote HER efficiency[32-34].

Regardless the interesting properties of TMDs, they are chemically inactive, hence development of facile and effective modification strategies in order to incorporate functional materials is necessary.[35,36] In this frame, exfoliated semiconducting MoS_2 and WS_2 were integrated with PCNDs, for the realization of a novel electron-donor system with interesting photophysical and redox properties.[16] The association of PCNDs to TMDs was based on the functionalization methodology of 1,2-dithiolanes which add at sulfur vacant sites located at the edges of TMDs.[37] Similarly, incorporation of PCNDs with MoS_2 by developing electrostatic interactions led to the formation of an electron-donor ensemble, while the electrocatalytic properties of the hybrid were tested towards HER, where it was found that after illumination the PCND/MoS_2 ensemble showed improved electrocatalytic activity.[38] However, the preparation of the aforementioned TMD/PCND hybrid materials was achieved by top-down strategies, namely based on exfoliated MoS_2 (or WS_2) followed by functionalization and coupling with PCNDs. On the contrary, bottom-up approaches for TMDs remain rather unexplored, while in the cases they have been employed the carbon nanodots conjugated have been prepared from carbonaceous[39] or graphitic[40-42] sources. Specifically, it has been demonstrated that hydrothermal treatment of carbonaceous CNDs, Na_2MoO_4 and L-cysteine resulted in the formation of MoS_2-CND.[39] Meanwhile, another electrocatalyst has been prepared by drop-casting GCNDs onto chemical vapor deposition grown MoS_2.[40] Moreover, by employing the latter preparation process, MoS_2-GCND has been obtained and charge-transfer between the two components was studied.[41,42]

Recently, we demonstrated an easy and fast protocol for the preparation of the metallic polytype MoS_2 from ammonium tetrathiomolybdate by employing microwave irradiation and the in-situ functionalization with poly(methacrylic) acid (PMAA). In the so-formed material, complexation of Mo atoms with the carboxylic acid units of PMAA takes place, yielding MoS_2-PMAA.[43] Functionalization of MoS_2 with PMAA significantly increased the solubility of MoS_2 in both aqueous and polar organic solvents, leading to stable dispersions for long time. Taking advantage of the aforementioned functionalization methodology, herein, we prepared a functional hybrid material consisting of MoS_2 and PCNDs. To the best of our knowledge; this is the first time that bottom-up synthesized MoS_2 and in-situ modified with PCNDs was screened as electrocatalyst towards HER. The electrocatalytic efficacy of MoS_2-PCND is compared with the hybrid material obtained by the covalent association of derivatized PCNDs with lipoic acid and exfoliated MoS_2.[16]

Results and Discussion

Adapting the recently reported protocol for the bottom-up preparation of MoS_2 and in-situ functionalization with species bearing carboxylic acid units,[43] we accomplished the fabrication of the MoS_2-PCND hybrid material. In more detail, thermal decomposition of ammonium tetrathiomolybdate under microwave irradiation conditions and in the presence of PCNDs featuring numerous carboxylic acids in the periphery, results on the formation of MoS_2 complexed with PCNDs according to Scheme 1. This approach involves a green and fast one-pot reaction, in which the functionalization of MoS_2 with PCNDs, via complexation of -COOH with Mo atoms, takes place during the preparation of the former. The so-formed MoS_2-PCND hybrid material is purified by filtration through a PTFE membrane (0.2 μm pore size) and extensive washing with dimethyl formamide and methanol. The particular work up procedure allows the removal of organic byproduct impurities and unreacted PCNDs as evidenced by the absence of any characteristic UV-Vis absorption bands in the filtrate.

10.1002/chem.202000125

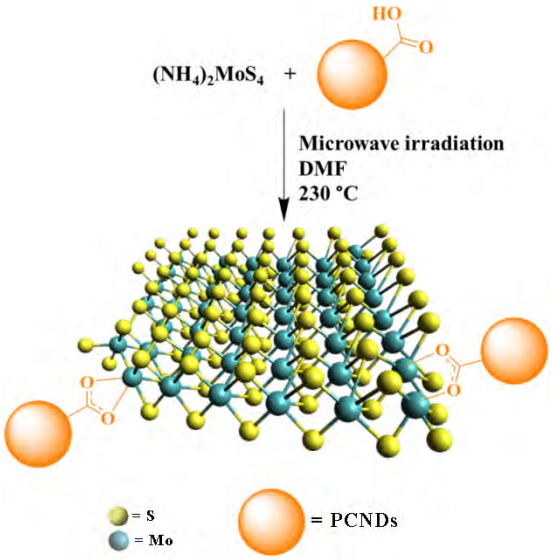

Scheme 1. Illustrative representation for the microwave-assisted preparation of MoS_2-PCND hybrid material.

The successful preparation of MoS_2-PCND is confirmed by diverse spectroscopic means. In particular, the ATR-IR spectrum of PCNDs shows the characteristic carbonyl vibration mode at 1705 cm^{-1} due to the surface -COOH units (Figure 1a). The particular band is found shifted to lower wavenumbers, at 1643 cm^{-1}, for MoS_2-PCND, due to complexation of the carboxylate species with the Mo atoms of MoS_2. Also, bands at 2855 and 2914 cm^{-1} are evident in the IR spectrum of the hybrid material, due to C-H vibration modes. To further support this argument a blank epperiment was conducted by mixing exfoliated MoS_2 and PCND. The IR spectrum of the blank material shows the characteristic carbonyl vibration mode at 1705 cm^{-1}, indicating that there is no complexation of PCNDs with Mo (Supporting Information, Figure S1). This is not surprising since complexation of Mo occurs with carboxylate and carboxylic acid species present in PCNDs. Hence, when PCNDs were treated under alkaline conditions inducing the realization of carboxylates, the IR spectrum of the blank material showed the corresponding vibration mode shifted at lower frequencies proving the efficient complexation with Mo. In addition, in the Raman spectrum of MoS_2-PCND, obtained upon excitation at 633 nm, characteristic modes due to MoS_2 are observed. Note that due to coupling with the A1 excitonic transition, which in turn produces resonance Raman enhancement of the first and second order vibrational modes, vibrational modes at 373, 404 and 452 cm^{-1} corresponding to the in-plane E^1_{2g}, out-of-plane A_{1g} and the 2LA(M) mode associated with disorder and defects,[44-46] are evident. Moreover, focusing on the lower wavenumber region, bands at 184 cm^{-1} as well as at 150, 224 and 325 cm^{-1} corresponding to vibrational modes A_{1g}(M)-LA(M), J_1, J_2 and J_3, respectively, are discernable. The latter J_1-J_3 phonon modes are fingerprints of the metallic polytype 1T-MoS_2,[44,47] thus their presence underscores the formation of the particular MoS_2 polytype in the course of the bottom-up approach. The suppression of the 2LA(M) band in the Raman spectrum of the MoS_2-PCND hybrid material, which is related to defect sites of MoS_2, as compared to the one of intact MoS_2, proves the effective functionalization of MoS_2 with PCNDs.[37] Moreover, the band at 285 cm^{-1} in the Raman spectrum of MoS_2-PCND, attributed to oxidized Mo states,[48,49] further verifies the successfull complexation of the carboxylate units present on the surface of the PCNDs with Mo.

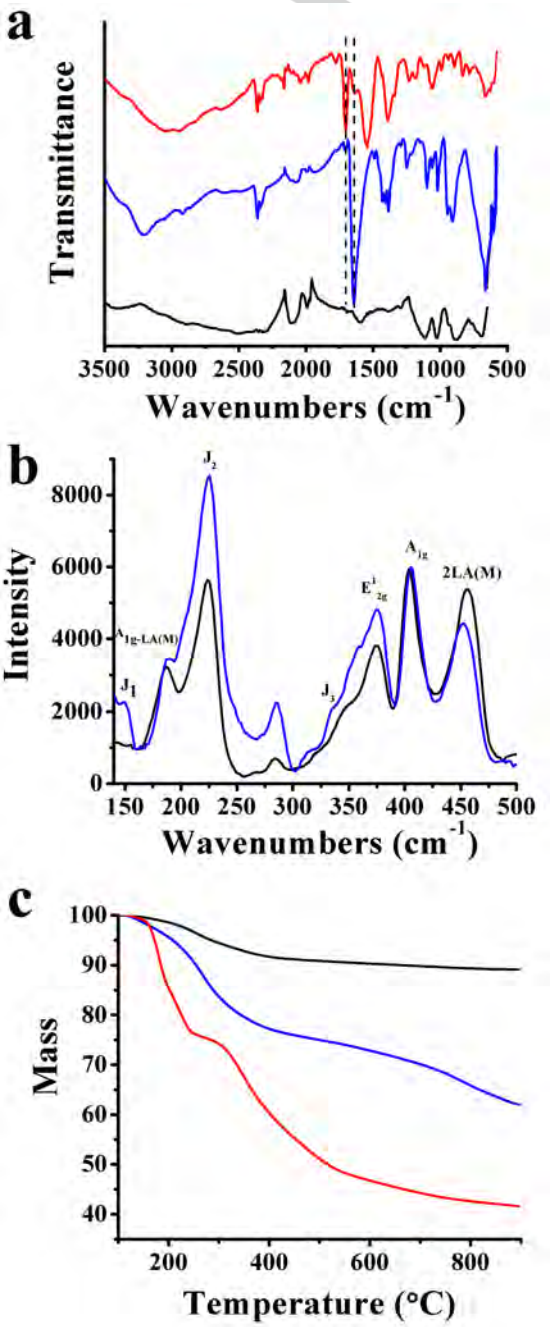

Figure 1. (a) ATR-IR spectra for MoS_2-PCND (blue), MoS_2 (black) and PCNDs (red). The vertical dotted lines are used as guides to observe the shift of the carbonyl vibration upon complexation with Mo. (b) Raman spectra (λ_{exc} 633

10.1002/chem.202000125

WILEY-VCH

nm) for MoS_2-PCND (blue) and MoS_2 (black). (c) TGA graphs for MoS_2-PCND (blue), MoS_2 (black) and PCNDs (red).

Thermogravimetric analysis (TGA) is employed for the evaluation of the PCNDs present in the MoS_2-PCND hybrid material. The thermograph of MoS_2 exhibits a mass loss of 4% up to 500°C due to the presence of defects, while PCNDs lose 48% of their mass at the temperature range 180-500°C due to their thermal decomposition. Thus, the 22% mass loss that is observed in the thermograph of MoS_2-PCNDs material in the same temperature region is attributed to the decomposition of the PCNDs within the hybrid. From the latter mass loss, the loading of PCNDs was calculated to be 1 per every 58 MoS_2 units.

The morphological characterization of the MoS_2-PCND hybrid material is performed by scanning transmission electron microscopy imaging. Low- and high-magnification HAADF-STEM images are displayed in Figure 2a and b. As it can be deduced from these micrographs, the structure of the material consists of curved agglomerates of MoS_2 flakes. Hence, HRSTEM electron energy loss spectroscopy (EELS) analysis, using the spectrum-image (SPIM) mode,[50, 51] is performed in the red squared area in HAADF-HRSTEM micrograph (Figure 2c). These results confirm the presence of Mo, S and C. Moreover, the presence of C in the whole scanned area indicates the high concentration of PCNDs within the MoS_2-PCND hybrid material.

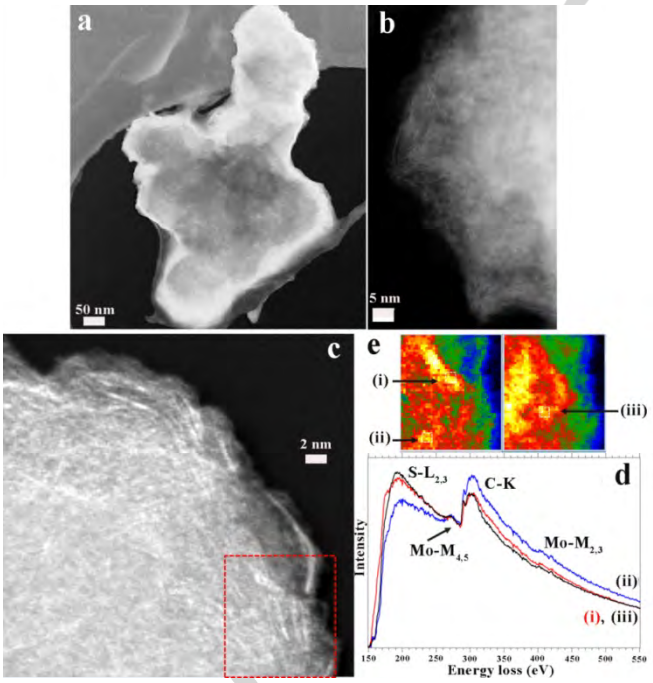

Figure 2. (a) Low- and (b) high-magnification HAADF-STEM images of MoS_2-PCND. (c) Agglomerates of MoS_2-PCND where an EELS spectrum-image (SPIM) has been recorded. (d) EEL spectra for regions (i), (ii) and (iii) shown in image (e) where each of these EEL spectra corresponds to the addition of 16 EEL spectra. (e) Chemical maps (Mo-$M_{4\text{-}5}$ on the left, and C-K on the right, respectively) extracted from EELS-SPIM shown in (c).

The photophysical properties of MoS_2-PCND are evaluated by absorption and photoluminescene spectroscopy, as shown in Figure 3a and b, respectively. Precisely, the absortion spectrum of PCNDs shows a band centered at 360 nm, while the absorption spectrum of MoS_2 shows a broad band at 350-500 nm nm. In the case of the hybrid material, the spectrum is governed by a broad band in the visible region of the electromagnetic spectrum, centered at 460 nm, resulting from the electronic communication between MoS_2 and PCNDs. In order to shed light in the electronic interactions at the excited state, fluorescence emission spectra are recorded for PCNDs and MoS_2-PCND upon exciation at 360 nm. In more detail, the photoluminesence spectrum of PCNDs reveals an emission band centered at 440 nm, while it is found blue-shifted at 430 nm in the spectrum of MoS_2-PCND. Furthermore, the emission intensity of PCNDs is found significantly quenched by the presence of MoS_2, for samples possessing matching absorbance at the excitation wavelength. The shift of the emission of PCNDs in the spectrum of the MoS_2-PCND hybrid material together with the simultaneous quenching reveals the development of electronic interactions between the two species within MoS_2-PCND at the excited state. This is to say that an alternative decay mechanism of the first excited state of PCNDs via dissipation to MoS_2-PCND occurs.

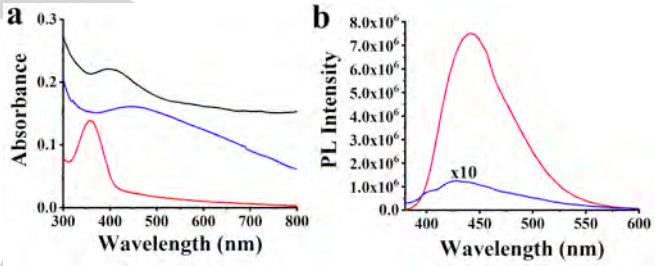

Figure 3. (a) Absorption and emission spectra for MoS_2 (black), PCNDs (red) and MoS_2-PCND (blue), obtained in DMF.

Time-correlated-single-photon-counting is employed to acquire the photoluminescence lifetime profile for MoS_2-PCND and to calculate the decay time of the first excited state of PCNDs (Supporting Information, Figure S2). Upon excitation of bare PCNDs at 376 nm, the emission at 440 nm is monoexponentially fitted, while analysis of the function reveals the fluorescence emission lifetime for bare PCNDs to be 9.3 ns. On the other hand, focusing on the emission of PCNDs in the MoS_2-PCND hybrid material, the photoluminescence decay is biexponentially fitted and analyzed with two different lifetimes of 1.6 and 5.9 ns. The slower decay lifetime, which is relatively close to that due to bare PCNDs, can be associated to non-interacting PCNDs with MoS_2 within MoS_2-PCND. Conversely, the faster lifetime is attributed to the decay of the single excited state of PCNDs through interactions with MoS_2. Moreover, the quenching rate constant (k^S_q) for the excited state of PCNDs and the quantum

yield (Φ^{S}_{q}) in MoS_2-PCND are calculated to be 5.175 x10^8 s^{-1} and 0.828, respectively.

Next, in order to examine the electrochemical properties of MoS_2-PCND against HER, linear sweep voltammetry measurements are performed by using a rotating-disc working glassy carbon electrode in a standard three-electrode glass cell at a scan rate of 5 mV/sec in nitrogen saturated 0.5 M aqueous sulfuric acid. Polarization curves of MoS_2-PCND, bare PCNDs and MoS_2 as well as commercially available Pt/C that are used as reference materials are shown in Figure 4a. For comparison reasons, a hybrid material prepared by the top-down approach that yields exfoliated semiconducting MoS_2 upon chlorosulfonic acid treatment of the bulk material[37] and functionalized with 1,2-dithiolane modified PCNDs,[16] abbreviated as MoS_2-PCND(exf-fun), is also screened. At this point, the following differences of MoS_2-PCND with MoS_2-PCND(exf-fun) should be noted: (a) preparation approach employed – bottom-up vs top-down, (b) MoS_2 polytype formed – metallic vs semiconducting, and (c) functionalization methodology – direct in-situ complexation vs 1,2-dithiolane addition.

Figure 4b displays tabulated values for the onset overpotential and the overpotential registered at -10 mA/cm^2 current density for all tested materials. Evidently, the onset potential for MoS_2-PCND is registered at -0.16 V vs RHE, which is more positive by 230 and 190 mV as compared to the value registered for bare MoS_2 (i.e. at -0.390 V) and MoS_2-PCND(exf-fun) (i.e. at -0.35 V), respectively. In addition, comparing the potential values at the current density of -10 mA/cm^2, which is the functional current density for electrochemical water splitting, sufficient hydrogen production and avoidance of misinterpretations from inherent electroactivity, it is found that MoS_2-PCND demonstrates higher electrocatalytic activity at -0.29 V vs RHE, shifted by 340 mV and 350 mV to more positive potentials compared to the value noted for intact MoS_2 (i.e. at -0.63 V) and MoS_2-PCND(exf-fun) (i.e. at -0.64 V), respectively. The superior electrocatalytic activity of MoS_2-PCND compared to MoS_2-PCND(exf-fun) is attributed to the increased active defect sites present in the bottom-up produced metallic MoS_2 compared to those present in the top-down exfoliated semiconducting MoS_2, where defect sites are located mostly at the periphery. Similar performance was observed in the case of metallic MoS_2 that were grown on graphene[32] and sulfur-doped graphene,[33] where the presence of the graphene conductive substrates improved the electrocatalytic activity of MoS_2 against HER. Analogously high electrocatalytic activity was also reported in the case of carbon supported amorphous Mo-based materials[52] and amorphous MoS_2 on nitrogen doped carbon.[53]

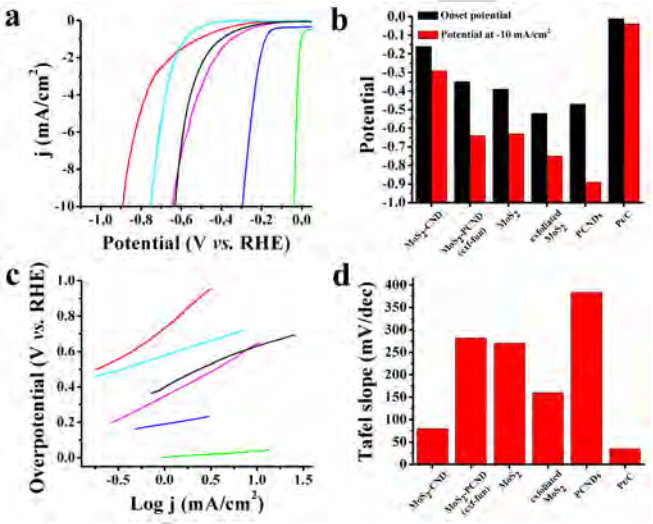

Figure 4. Linear sweep voltammograms (LSVs) for HER of MoS_2-PCND (blue), MoS_2-PCND(exf-fun) (pink), bare MoS_2 (black), exfoliated MoS_2 (cyan), PCNDs (red), and Pt/C (green). (b) Tabulated graphs for onset overpotential and overpotential value registered at -10 mA/cm^2 current density for all tested materials. (c) Tafel slope values for MoS_2-PCND (blue), MoS_2-PCND(exf-fun) (pink), bare MoS_2 (black), exfoliated MoS_2 (cyan), PCNDs (red), and Pt/C (green). (d) Tabulated Tafel slope values for all tested materials. LSV polarization curves were obtained in a nitrogen saturated aqueous 0.5 M H_2SO_4 electrolyte, at a rotation speed of 1,600 rpm and a scan rate of 5 mV/s.

Furthermore, in order to decode the superior electrocatalytic behavior of MoS_2-PCND and determine the rate-limiting step for HER, Tafel slopes are extracted from the polarization curves for all tested materials (Figure 4c). Further analysis shows that bare MoS_2 and PCNDs, screened as reference materials, exhibit high Tafel values of 390 and 270 mV/dec, respectively. In addition, the Tafel value for MoS_2-PCND(exf-fun) is also high, 282 mV/dec. Such high Tafel values reveal that the rate-limiting step for HER for bare MoS_2 and PCNDs as well as MoS_2-PCND(exf-fun) is the initial adsorption of a proton onto the electrode surface via a reduction process (Volmer adsorption). Conversely, MoS_2-PCND shows a much lower Tafel slope value of 80 mV/sec, slightly higher than that due to Pt/C (i.e. 35 mV/dec), which manifests that HER is rate-limited by the electrochemical desorption of adsorbed hydrogen atoms onto the modified electrode to generate hydrogen (Heyrovsky desorption). This improvement shows that the hydrogen adsorption ability of MoS_2 is enhanced by the presence of PCNDs, implying improvement of the accessibility and/or reactivity of protons and water to electrochemically active sites.[3] Such a Tafel slope value for

MoS_2-PCND comes in excellent agreement with the improved electrocatalytic reaction deriving from the LSV curves, since lower Tafel slope value suggests that for the generation of a certain current only a lower overpotential is required.

$H_3O^+ + e^- \rightarrow H_{ads} + H_2O$ (Volmer adsorption)

$H_{ads} + H_3O^+ + e^- \rightarrow H_2 + H_2O$ (Heyrovsky desorption)

$H_{ads} + H_{ads} \rightarrow H_2$ (Tafel desorption)

In order to better understand the fluent charge transport in MoS_2-PCND the electrochemically active surface area (ECSA) was calculated according to the equation ECSA = C_{dl}/C_s, where C_{dl} is the electrochemical double-layer capacitance and C_s is the specific capacitance of a flat surface with 1 cm^2 of real surface area with a value assumed to be 40 μF/cm^2 for the flat electrode. Along these lines, cyclic voltamograms in a non-Faradaic region are measured at scan rates of 50, 100, 200, 300, 400 and 500 mV/sec, (Supporting Information, Figure S3) in order to estimate the ECSA value from the C_{dl} by plotting the Δj = (j_a-j_c) at a potential value vs RHE as a function of the scan rate according to the equation $C_{dl} = (\Delta j)/2dV_b$. Specifically, the MoS_2-PCND hybrid material shows the higher ECSA value of around 43.5 cm^2, while the equivalent value that is noted for MoS_2-PCND(exf-fun) is significantly lower at 2.1 cm^2. Similarly, the ECSA values that are estimated for the rest reference materials are considerably lower than the one registered for MoS_2-PCND (Table 1). These findings are in line with the electrocatalytic results towards HER, since higher ECSA values are related with more effective accessibility of the active sites.

Moreover, the long-term stability of MoS_2-PCND is evaluated by performing durability studies. Figure 5 shows LSV polarization curves for MoS_2-PCND as compared to that for MoS_2-PCND(exf-fun) as well as for Pt/C employed as reference, after continuous cycling for 2,000 cycles, where negligible loss of the cathodic current is noted for all tested materials. The long-term stability for the rest materials is presented in the supporting information section as Figure S4. Table 1 summarizes the various HER parameters for all screened materials, before and after 2,000 cycles.

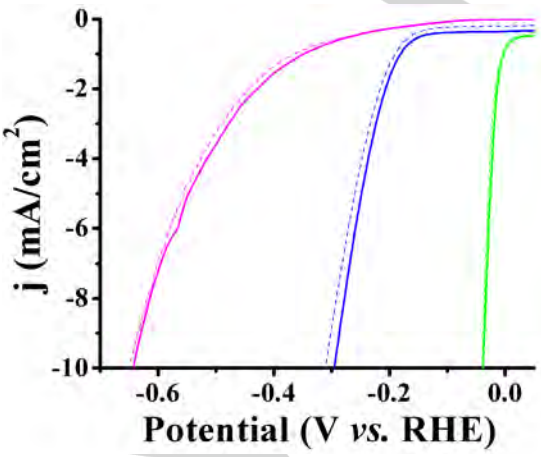

Figure 5. LSV for HER of (a) MoS_2-PCND (blue), MoS_2-PCND(exf-fun) (pink) and Pt/C (green) before (solid) and after 2,000 cycles (dashed). The LSV polarization curves were obtained in nitrogen-saturated aqueous 0.5 M H_2SO_4 electrolyte, at a rotation speed of 1,600 rpm and a scan rate of 5 mV/s.

Table 1. Electrochemical parameters for HER.

Catalyst	Onset overpotential (V vs. RHE)	Overpotential (V vs. RHE) at -10 mA/cm^2	Tafel slope (mV/dec)	ECSA (cm^2)
MoS_2-PCND	0.16	0.29	80	~43.5
MoS_2-PCND[a]	0.17	0.31	84	-
MoS_2-PCND (exf-fun.)	0.35	0.64	282	~2.1
MoS_2-PCND (exf-fun)[a]	0.37	0.65	282	-
bottom-up synthesized MoS_2	0.39	0.63	271	~ 2.25
bottom-up synthesized MoS_2[a]	0.39	0.69	240	-
exfoliated MoS_2	0.52	0.75	160	~ 0.88
exfoliated MoS_2[a]	0.55	0.76	163	-
PCNDs	0.47	0.89	384	~ 0.39
PCNDs[a]	0.57	0.94	353	-
Pt/C	0.011	0.038	35	-
Pt/C[a]	0.011	0.038	35	-

[a]After 2,000 cycles.

Conclusions

In conclusion, we presented a new facile and fast bottom-up approach to prepare an efficient electrocatalyst for HER consisting of MoS_2 and PCNDs for the first time. Specifically, the MoS_2-PCND material was formed by the thermal decomposition of the ammonium tetrathiomolybdate and the in-situ complexation of Mo with the carboxylic acid units of PCNDs. TEM imaging coupled with EELS along with complementary spectroscopic techniques confirmed the successful preparation of the hybrid material, while photoluminescence and time-resolved florescence studies validated the charge/energy transfer from PCNDs to MoS_2 at the excited state. MoS_2-PCND electrocatalyst showed superior activity towards HER and outperformed the MoS_2-PCND(exf-fun) corresponding material acquired by a top-down approach. Moreover, MoS_2-PCND showed a low Tafel slope and a significantly higher ECSA value than MoS_2 and MoS_2-PCND(exf-fun) which indicates the existence of larger functioning catalytic active sites. The efficient charge/energy transfer from PCNDs to MoS_2, the highly active defect MoS_2 sites and the synergetic effect between the two components within the hybrid material, not only granted the improvement of the catalytic activity of MoS_2 but also ensured a

more efficient hydrogen production over its semiconducting hybrid counterpart. Finally, this work reveals a novel bottom-up synthetic approach for the preparation of highly active electrocatalysts for HER that can be applied for the functionalization of diverse TMDs with various organic/inorganic materials as donor-acceptor systems.

Experimental Section

General. Chemicals, reagents, and solvents were purchased from Sigma-Aldrich and used as received. Infrared (IR) spectra were acquired on a Fourier Transform IR spectrometer (Equinox 55 from Bruker Optics) equipped with a single reflection diamond ATR accessory (DuraSamp1IR II by SensIR Technologies). Electronic absorption spectra (UV-Vis) were recorded on a PerkinElmer (Lambda 19) UV-Vis-NIR spectrophotometer. UV-Vis spectra of films were obtained in transmission mode using a Shimadzu UV-2401 PC spectrometer. Steady-state emission spectra were recorded on a Fluorolog-3 Jobin Yvon-Spex spectrofluorometer (model GL3-21). Thermogravimetric analysis was performed using a TGA Q500 V20.2 Build 27 instrument by TA in a nitrogen (purity >99.999%) inert atmosphere. TEM samples were prepared by drop-casting a suspension containing the hybrid materials on Cu grids coated with a holey carbon membrane. High-angle annular dark-field scanning-transmission electron (HAADF-STEM) imaging and electron-energy loss spectroscopy (EELS) were acquired in a probe-corrected FEI Titan Low-Base microscope fitted with a X-FEG® gun and Cs-probe corrector CESCOR from CEOS GmbH and operated at 80 keV (convergent semi-angle of 25 mrad). Electrochemical measurements were carried out at room temperature in N_2-saturated 0.5 M H_2SO_4 in a standard three-compartment electrochemical cell by using a Metrohm potensiostat/galvanostat (Model Autolab PGSTAT128N). Platinum wire was used as a counter-electrode and as reference an $Hg/HgSO_4$ (0.5 M K_2SO_4) electrode was placed into a Luggin capillary. Potentials were corrected according to E vs RHE = E vs $Hg/HgSO_4$ + 0.680. The working electrode was a RDE with glassy carbon disk (geometric surface area: 0.0196 cm^2). Linear sweep voltammetry measurements were conducted with a scan rate of 5 mV/s. To prepare the catalyst ink, 4.0 mg of the hybrid catalytic powder were dispersed in a mixture of solvents (1 mL) containing water, isopropanol, and 5% Nafion (v/v/v=4:1:0.02) and sonicated for 30 min. The working electrode was first cleaned through polishing by 6, 3 and 1mm diamond pastes, rinsed with deionized water, and sonicated in double-distilled water. Then, 8.5 µL aliquots of the catalyst ink were casted on the electrode surface and dried at room temperature.

Preparation of PCNDs. 2.0 g citric acid monohydrates (9.5 mmol) were dissolved in 15 mL of ultrapure water. Upon addition of 0.64 mL of EDA (1 equiv), the solution was heated up to 140°C through microwave irradiation (stirring, open vessel), provoking the evaporation of the water. The temperature was kept constant for 1 min; after that, the irradiation was stopped and the mixture redissolved in 10 mL of water. The same process was repeated two more times, for a total of 3 min at 140°C. The solid product was diluted with ultrapure water, filtrated through a 0.45 µm PTFE membrane, and dialyzed against ultrapure water (MWCO = 0.5−1.0 kDa, 3 days, twice a day), yielding a brownish powder with a yield in mass of 35%.

Preparation of MoS_2-PCND. The MoS_2-PCND hybrid material was synthesized by microwave irradiation. Briefly, 10 mg of $(NH_4)_2MoS_4$ were diluted in 3 mL DMF and sonicated for 30 minutes. Afterwards, 10 mg of PCNDs were added and the mixture underwent microwave treatment for 2 hours at 230°C. The dispersion was filtered over PTFE filter (pore size 0.2 µm) and washed with a small amount of DMF and methanol. The solid residue was collected to obtain the MoS_2-PCND material. It should be noted that the methodology can be scaled up depending on the microwave instrumentation and by using bigger reaction vessels.

Acknowledgements

This project has received funding from the European Union's Horizon 2020 research and innovation programme under the Marie Sklodowska-Curie grant agreement N° 642742. Support of this work by the project "Advanced Materials and Devices" (MIS 5002409) which is implemented under the "Action for the Strategic Development on the Research and Technological Sector", which is implemented under the "Reinforcement of the Research and Innovation Infrastructures", funded by the Operational Program "Competitiveness, Entrepreneurship and Innovation" (NSRF 2014-2020) and co-financed by Ministry of Development and Investments, Greece, and the European Union (European Regional Development Fund) is also acknowledged. A.M.B. and W.K.M. acknowledge Spanish MINEICO (project grant ENE2016-79282-C5-1-R, AEI/FEDER, UE) and the Gobierno de Aragón (Grupo Reconocido DGA T03_17R, FEDER, UE). The SR-EELS studies were conducted at the Laboratorio de Microscopias Avanzadas, Instituto de Nanociencia de Aragon, Universidad de Zaragoza, Spain. The SR-EELS studies were conducted at the Laboratorio de Microscopias Avanzadas, Instituto de Nanociencia de Aragon, Universidad de Zaragoza, Spain. R.A. gratefully acknowledges the support from the Spanish Ministry of Economy and Competitiveness (MINECO) through project grant MAT2016-79776-P (AEI/FEDER, UE) from the Government of Aragon and the European Social Fund under the project "Construyendo Europa desde Aragon" 2014-2020 (grant number E13_17R) and from the European Union H2020 programs "ESTEEM3" (823717) and under the "Graphene Flagship" CORE2 project grant agreement No 785219.

Keywords: transition metal dichalcogenides • bottom-up preparation • polymer carbon nanodots • functionalization • electrocatalysis

[1] N. Dubouis, A. Grimaud, *Chem. Sci.* **2019**, *10*, 9165-9181.

[2] W. Li, D. Xiong, X. Gao, L. Liu, *Chem. Commun.* **2019**, 55, 8744-8763.

[3] Y. Chen, K. Yang, B. Jiang, J. Li, M. Zeng, L. Fu, *J. Mater. Chem. A* **2017**, *5*, 8187-8208.

[4] C. Xia, S. Zhu, T. Feng, M. Yang, B. Yang, *Adv. Sci.* **2019**, *6*, 1901316.

[5] J. T. Margraf, F. Lodermeyer, V. Strauss, P. Haines, J. Walter, W. Peukert, R. D. Costa, T. Clark, D. M. Guldi, *Nanoscale Horiz.* **2016**, *1*, 220-226.

[6] B. C. M. Martindale, E. Joliat, C. Bachmann, R. Alberto, E. Reisner, *Angew. Chem. Int. Ed.* **2016**, *55*, 9402-9406.

[7] K. K. R. Datta, G. Qi, R. Zboril, E. P. Giannelis, *J. Mater. Chem. C* **2016** *4*, 9798-9803

[8] J. Gu, D. Hu, J. Huang, X. Huang, Q. Zhang, X. Jia, K. Xi, *Nanoscale* **2016**, *8*, 3973-3981.

[9] R. Das, R. Bandyopadhyay, P. Pramanik, *Mater. Today Chem.* **2018**, *8*, 96-109.

[10] S. Zhu, Y. Song, J. Shao, X. Zhao, B. Yang, *Angew. Chem. Int. Ed.* **2015**, *54*, 14626-14637.

[11] S. Zhu, Q. Meng, L. Wang, J. Zhang, Y. Song, H. Jin, K. Zhang, H. Sun, H. Wang, B. Yang, *Angew. Chem. Int. Ed.* **2013**, *52*, 3953-3957.

[12] S. Tao, S. Lu, Y. Geng, S. Zhu, S. A. T. Redfern, Y. Song, T. Feng, W. Xu, B. Yang, *Angew. Chem. Int. Ed.* 2018, *57*, 2393-2398.

[13] M. Yavari, M. Mazloum-Ardakani, S. Gholipour, N. Marinova, J. L. Delgado, S. ‐ H. Turren ‐ Cruz, K. Domanski, N. Taghavinia, M. Saliba, M. Grätzel, A. Hagfeldt, W. Tress, *Adv. Energy Mater.* **2018**, *8*, 1702719.

[14] L. Vallan, E. P.Urriolabeitia, A. M. Benito, W. K. Maser, *Polymer* **2019**, *177*, 97-101.

[15] L. Vallan, E. P. Urriolabeitia, F. Ruiperez, J. M. Matxain, R. Canton-Vitoria, N. Tagmatarchis, A. M. Benito, W. K. Maser, *J. Am. Chem. Soc.* **2018**, 140, 12862-12869.

[16] L. Vallan, R. Canton-Vitoria, H. B. Gobeze, Y. Jang, R. Arenal, A. M. Benito, W. K. Maser, F. D'Souza, N. Tagmatarchis, *J. Am. Chem. Soc.* **2018**, 140, 13488-13496.

[17] T. Feng, S. Zhu, Q. Zeng, S. Lun, S. Tao, J. Liu, B. Yang, *ACS Appl. Mater. Interfaces* **2018**, *10*, 12262-12277.

[18] W. Zhang X. Liao, X. Pan, M. Yan, Y. Li, X. Tian, Y. Zhao, L. Xu, L. Mai, *Small* **2019**, *15*, 1900964.

[19] P. Gnanasekar, D. Periyanagounder, J. Kulandaivel, *Nanoscale* **2019**, *11*, 2439-2446.

[20] S. Bolar, S. Shit, J. S. Kumar, N. C. Murmu, R. S. Ganesh, H. Inokawa, T. Kuila, *Appl. Catal. B Environ.* **2019**, *254*, 432-442.

[21] S. Bolar, S. Shit, J. S. Kumar, N. C. Murmu, R. S. Ganesh, H. Inokawa, T. Kuila, *Appl. Catal. B.* **2019**, *254*, 432-442.

[22] W. Choi, N. Choudhary, G. H. Han, J. Park, D. Akinwande, Y. H. Lee, *Mater. Today* **2017**, *20*, 116-130.

[23] J. Hu, C. Zhang, X. Meng, H. Lin, C. Hu, X. Long, S. Yang, *J. Mater. Chem. A* **2017**, *5*, 5995-6012.

[24] Y. B. Lee, S. K. Kim, S. Ji, W. Song, H.-S. Chung, M. K. Choi, M. Lee, S. Myung, J. Lim, K.-S. An, S. S. Lee, *J. Mater. Chem. A* **2019**, *7*, 3563-3569.

[25] Z. Zhang, Y. Wang, X. Leng, V. H. Crespi, F. Kang, R. Lv, *ACS Appl. Energy Mater.* **2018**, 1, 1268-1275.

[26] Y. Li, K. Yin, L. Wang, X. Lu, Y. Zhang, Y. Liu, D. Yan, Y. Song, S. Luo, *Appl. Catal. B.* **2018**, *239*, 537-544.

[27] Y. Zhang, Y. Kuwahara, K. Mori, H. Yamashita, *Chem. Asian J.* **2018**, *14*, 278-285.

[28] G. Ye, Y. Gong, J. Lin, B. Li, Y. He, S. T. Pantelides, W. Zhou, R. Vajtai, P. M. Ajayan, *Nano Lett.* **2016**, *16*, 1097-1103.

[29] Y. Jiao, A. M. Hafez, D. Cao, A. Mukhopadhyay, Y. Ma, H. Zhu, *Small* **2018**, *14*, 1800640.

[30] D. Voiry, M. Salehi, R. Silva, T. Fujita, M. Chen, T. Asefa, V. B. Shenoy, G. Eda and M. Chhowalla, *Nano Letters* **2013**, *13*, 6222-6227.

[31] M. A. Lukowski, A. S. Daniel, F. Meng, A. Forticaux, L. Li, S. Jin, *J. Am. Chem. Soc.* **2013**, *135*, 10274-10277.

[32] A. Kagkoura, I. Tzanidis, V. Dracopoulos, N. Tagmatarchis, D. Tasis, *Chem. Commun.* **2019**, *55*, 2078-2081.

[33] A. Kagkoura, M. Pelaez-Fernandez, R. Arenal, N. Tagmatarchis, *Nanoscale Adv.* **2019**, *1*, 1489-1496.

[34] A. Kagkoura, T. Skaltsas, N. Tagmatarchis, *Chem. Eur. J.* **2017**, *23*, 12967-12979.

[35] A. Stergiou, N. Tagmatarchis, *Chem. Eur. J.* **2018**, *24*, 18246-18257.

[36] D. K. Perivoliotis, N. Tagmatarchis, *Carbon* **2017**, *118*, 493-510.

[37] R. Canton-Vitoria, Y. Sayed-Ahmad-Baraza, M. Pelaez-Fernandez, R. Arenal, C. Bittencourt, C. P. Ewels, N. Tagmatarchis, *NPJ. 2D Mater. Appl.* **2017**, *1*, 13.

[38] R. Canton-Vitoria, L. Vallan, E. Urriolabeitía, A. M. Benito, W. K. Maser, N. Tagmatarchis, *Chem. Eur. J.* **2018**, *24*, 10468-10474.

[39] S. Zhao, C. Li, L. Wang, N. Liu, S. Qiao, B. Liu, H. Huang, Y. Liu, Z. Kang, *Carbon* **2016**, *99*, 599-606.

[40] B. Guo, K. Yu, H. Li, R. Qi, Y. Zhang, H. Song, Z. Tang, Z. Zhu, M. Chen, *ACS Appl. Mater. Interfaces* **2017**, *9*, 3653-3660.

[41] Z. Li, R. Ye, R. Feng, Y. Kang, X. Zhu, J. M. Tour, Z. Fang, *Adv. Mater.* **2015**, 27, 5235-5240.

[42] C. Chen, H. Qiao, S. Lin, C. M. Luk, Y. Liu, Z. Xu, J. Song, Y. Xue, D. Li, J. Yuan, W. Yu, C. Pan, S. P. Lau, Q. Bao, *Sci. Rep.* **2015**, 5, 11830.

[43] A. Kagkoura, T. Sentoukas, Y. Nakanishi, H. Shinohara, S. Pispas, N. Tagmatarchis, *Chem. Phys. Lett.* **2019**, *716*, 1-5.

[44] G. Pagona, C. Bittencourt, R. Arenal, N. Tagmatarchis, *Chem. Commun.* **2015**, *51*, 12950-12953.

[45] H. Li, Q. Zhang, C. C. R. Yap, B. K. Tay, T. H. T. Edwin, A. Olivier, D. Baillargeat, *Adv. Funct. Mater.* **2012**, *22*, 1385-1390.

[46] S.-L. Li, H. Miyazaki, H. Song, H. Kuramochi, S. Nakaharai, K. Tsukagoshi, *ACS Nano* **2012**, 6, 7381-7388.

[47] A. P. Nayak, T. Pandey, D. Voiry, J. Liu, S.T. Moran, A. Sharma, C. Tan, C.-H. Chen, L.-J. Li, M. Chhowalla, J.-F. Lin, A.K. Singh, D. Akinwande, *Nano Lett.* **2015**, *15*, 346-353.

[48] L. Aleksandrov, T. Komatsu, R. Iordanova, Y. Dimitriev, *J. Phys. Chem. Solids* **2011**, *72*, 263-268.

[49] B. C. Windom, W. G. Sawyer, D. W. Hahn, *Tribol. Lett.* **2011**, *42*, 301-310.

[50] R. Arenal, F.de la Peña, O. Stéphan, M. Walls, M. Tencé, A. Loiseau, C. Colliex, *Ultramicroscopy* **2008**, *109*, 32-38.

[51] R. Arenal. X. Blase, A. Loiseau, *Adv. Phys.* **2010**, *59*, 101-179.

[52] J. Guo, J. Wang, Z. Wu, W. Lei, J. Zhu, K. Xia, D. Wang, *J. Mater. Chem. A*, **2017**, *5*, 4879-4885.

[53] S. Lu, W. Wang, S. Yang, W. Chen, Z. Zhuang, W. Tang, C. He, J. Qian, D. Ma, Y. Yang, S. Huang, *Nano Res.* **2019**, *12*, 3116-3122.